IN-FLIGHT VIBRATION-BASED STRUCTURAL HEALTH MONITORING OF AIRCRAFT WINGS

Eugen Neu *,**, **Frank Janser** **, **Akbar A. Khatibi** *, **Adrian C. Orifici** *
* RMIT University, Australia, ** FH Aachen UAS, Germany

Keywords: *structural health monitoring, operational modal analysis, operational variability*

Abstract

This work presents a methodology for automated damage-sensitive feature extraction and anomaly detection under multivariate operational variability for in-flight assessment of wings. The method uses a passive excitation approach, i. e. without the need for artificial actuation. The modal system properties (natural frequencies and damping ratios) are used as damage-sensitive features. Special emphasis is placed on the use of Fiber Bragg Grating (FBG) sensing technology and the consideration of Operational and Environmental Variability (OEV). Measurements from a wind tunnel investigation with a composite cantilever equipped with FBG and piezoelectric sensors are used to successfully detect an impact damage. In addition, the feasibility of damage localisation and severity estimation is evaluated based on the coupling found between damage- and OEV-induced feature changes.

Introduction

The longtime vision for vibration-based Structural Health Monitoring (SHM) in aeronautical engineering is the fully automatic supervision of vital aircraft components that are exposed to possibly critical operational or impact loads. The most critical component of every SHM system are the damage-sensitive features. They ultimately determine the damage-sensitivity of the overall system as well as its noise rejection capabilities and robustness [1]. The best investigated and understood dynamic system properties are modal parameters, which also have been shown to be damage-sensitive in an uncounted number of studies. Operational Modal Analysis (OMA) techniques can be used to extract modal parameters from systems that are excited by unmeasured forces and have been suggested as part of SHM systems in civil engineering [2]. This theoretically opens the opportunity for continuous in-flight wing monitoring. However, improvements across a range of critical areas are needed before SHM of aircraft wings can become a reality. These include particularly the robust automatization of OMA, the consideration of wind-related Operational and Environmental Variability (OEV), sensor robustness and sensitivity and the systematic application of statistical pattern recognition methods.

The current damage condition of a system can be evaluated in five distinct levels [3]. A comparison between an actual measurement of damage-sensitive features and an undamaged reference state will allow for damage detection (I) and localization (II). Adding information about the system's damage dependent behavior will further allow for damage classification (III) and severity estimation (IV). Remaining lifetime forecasting (V) is conceivable, provided measurements of the current system state, future loading estimations and damage propagation models are available. The levels (I) and (II) can be evaluated solely from measurements of the undamaged system. Here the goal is to determine whether the current system state is abnormal. To assess higher SHM levels samples of every critical damage scenario are required. In this case the challenge is to determine whether a damage scenario or the undamaged ref-

erence state best describes the currently measured system behavior. In machine learning these two types of problems are known as unsupervised and supervised learning scenarios.

This paper introduces an algorithm for automated vibration-based damage detection (I) that is developed for in-flight assessment of wings. The procedure includes an Automated Operational Modal Analysis (AOMA) algorithm for damage-sensitive feature extraction and automated baseline set preparation[1]. The procedure only requires one user-defined parameter. All other internal parameters are obtained from the actual data through clustering and statistical modelling. The algorithm is applied to data of a wind tunnel experiment with a cantilever that was subjected to an impact load. Damage detection is investigated under OEV. Furthermore, the data, together with a Finite Element Method (FEM) model, are used to discuss the feasibility of damage localisation (II) and severity estimation (III) and their application to aircraft wings.

Methodology

Experimental setup and data

The investigation was conducted in a closed-loop wind tunnel with an open test section. The investigated specimen was a glass fiber-reinforced polymer plate (500 mm × 90 mm × 4 mm), which was subjected to different flow conditions. The structural response of the specimen was measured using three sensor types: Fiber Bragg Grating (FBG) sensors, a unidirectional piezoelectric accelerometer and a piezoelectric strain sensor. The setup is shown in figure 1. Further information about the experiment were published in [4].

Three Angle Of Attack (AOA) $\alpha_{1...3} = 0°$, $1°$, $2°$ and three inflow velocities $v_{1...3} = 70\,\text{km/h}$, $100\,\text{km/h}$, $130\,\text{km/h}$ were investigated. Furthermore, three mass configurations were investigated: No additional mass (m_0), a 16 g mass at the upper attachment point (m_1), a second 16 g

---

[1]The AOMA algorithm and the baseline preparation algorithm are separately described and discussed in two papers that are currently under review. The drafts can be obtained from the lead author.
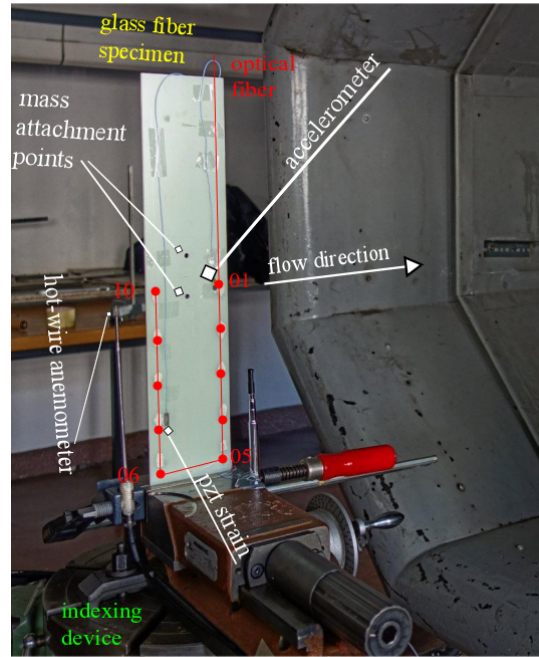

Figure 1: Wind tunnel setup.

mass at the lower attachment point (m_2). All measurements were repeated after an impact damage was introduced to the specimen. In total 54 individual operation points were investigated. Measurements were conducted for approximately 40 minutes at every operation point and split into 64 equally sized datasets per operation point.

The impact damage is shown in figure 2. It was created with a drop test rig. The 20 J impact resulted in a palpable dent on the impact side and clearly visible fiber breakage on the opposite side. The damage was introduced at the symmetry plane of the specimen, placed at the height of the piezoelectric strain sensor. The former location of the sensor is indicated with red.

Figure 2: Impact damage (white cross).

Figure 3 shows the geometry of the FEM model that was used to study the effect of varying damage types and severities. Path A and B were

placed at the positions of the FBG fiber (see figure 1). Two damage scenarios were investigated: 1) The layers in the affected region were allowed to slide but not to separate or penetrate each other. 2) A Young's modulus and shear modulus reduction in the affected region. The first damage type represents pure delamination whereas the second type represents a general degeneration of the specimen in the affected region. Both damage scenarios can be represented with linear theory and are therefore suitable for classic numerical modal analysis. The commercial software suite ANSYS was used for the numerical investigation.
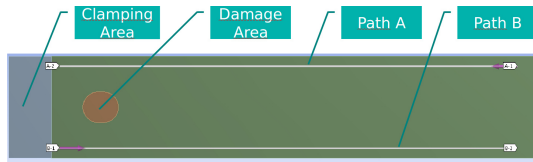

Figure 3: Numerical model.

Automated OMA

The OMA procedure used in this work is the data-driven Stochastic Subspace Identification - Canonical Variate Analysis method [5]. The essential concept is that the algorithm expects a single input parameter (the model order n), and responses with n sets of modal properties (in the OMA case n poles $\lambda_1 \ldots \lambda_n$ and n unscaled mode shapes $\boldsymbol{\phi}_1 \ldots \boldsymbol{\phi}_n$). Since the number of modes is controlled by an input parameter, a procedure is needed to separate the physical modes from the fictitious modes that fill the open spaces. The proposed procedure starts with identifications from a large number of model orders $n = \{n_{min}, 4, 6, \ldots, n_{max}\}$.

Whether a mode represents a physical mode or a fictitious mode can usually not be deduced from its isolated modal properties. However, there are Hard Validation Criteria (HVC) that indicate certainly fictitious modes [6]. Stable systems do not have negative damping. Poles without imaginary part do not represent a system capable of oscillation. Physical poles always occur in complex conjugate pairs at a single model order n. Poles that meet this criteria are removed immediately.

Nearest neighbours

The primary characteristic of physical modes, which distinguishes them from fictitious ones, is their similarity to their siblings at other model orders. First, for each mode the nearest neighbour from the next higher order is found. The algorithm starts with the lowest model order and calculates the distances between each mode $\lambda_{n,i}, \boldsymbol{\phi}_{n,i}$ in the current model order and all modes in the next model order $\lambda_{n+1,j}, \boldsymbol{\phi}_{n+1,j}$. The distance between two modes can be measured in a variety of ways, here the sum of normalized pole distance and Modal Assurance Criterion (MAC) is used:

$$dpMAC_{i,j} = \frac{\left|\lambda_i - \lambda_j\right|}{\max(|\lambda_i|, |\lambda_j|)} + \left(1 - MAC_{i,j}\right) \quad (1)$$

The neighbours for the last model order n_{max} are found from the first model order n_{min}. The final result of the procedure is the nearest neighbour for each mode and the dpMAC distance between the two.

K-means fictitious pole removal

The nearest-neighbour-information is used to create a Soft Validation Criteria (SVC)-vector [6] for subsequent separation into probably physical and certainly fictitious modes (Eq. (2)).

$$\mathbf{p_i} = [\, d\lambda_{i,j} \; df_{ui,j} \; d\xi_{i,j} \; (1 - MAC_{i,j}) \; dMPD_{i,j} \,]^T \quad (2)$$

The SVC-vector consists of the relative eigenvalue difference $d\lambda$, the relative natural frequency difference df, the relative damping ratio difference $d\xi$, the Modal Assurance Criterion MAC and the Mean Phase Deviation MPD [6]. In this form the vector only has one informative value, namely the proximity to the nearest neighbour and the shape of every variable resembles the same probability distribution.

The nearest-neighbor detection process results in heavily skewed feature distributions. Thus, the feature vector is transformed into a shape that more resembles a normal distribution using the approach described in [7]. A final normalisation to standard scores (z-score) is applied to the feature vector, to give every variable equal weight.

The goal of k-means clustering is to minimise the within-cluster sum of squares (Eq. (3)).

$$\{S_1, S_2\} = \arg\min_S \sum_{k=1}^{2} \sum_{\mathbf{h}_{N,i} \in S_k} \|\mathbf{h}_{N,i} - \boldsymbol{\mu}_k\|^2 \quad (3)$$

Equation (3) returns two sets, S_1 and S_2, which contain the probably physical and the certainly fictitious modes. $\boldsymbol{h}_{N,i}$ is the transformed and normalized feature vector. $\boldsymbol{\mu}_1$ and $\boldsymbol{\mu}_2$ are the centroids of the sets S_1 and S_2 and are initialized with $+\sigma(\boldsymbol{h}_{N,i})$ and $-\sigma(\boldsymbol{h}_{N,i})$ respectively.

Hierarchical clustering

Hierarchical clustering is used to aggregate similar modes from different model orders into clusters. The distances are measured according to Eq. (1). The idea behind the application of hierarchical clustering to AOMA is to stop the clustering process when the distance between the nearest two clusters is larger than a certain threshold. Often such thresholds are user-defined. However, here the inverse cumulative Weibull distribution function is used to find the 95th percentile of the probably physical modes

$$P\left(dpMAC_{PP,i,j} \leq \tilde{d}_{dpMAC}\right) = 0.95 \quad (4)$$

where $\tilde{d}_{dpMAC}$ is the 95th percentile threshold and $dpMAC_{PP,i,j}$ is the distance between two neighbours from different model orders.

In addition to the distance between individual modes, the distance between multi-member clusters also needs to be evaluated. A number of different linkage methods are available [8]. Here average linkage (Eq. (5)) is used, where the distance $d_{r,s}$ between two clusters is defined as the average distance between all members of one cluster to all members of another cluster.

$$d_{r,s} = \frac{1}{n_r n_s} \sum_{i=1}^{n_r} \sum_{j=1}^{n_s} \text{dist}\left(x_{ri}, x_{sj}\right) \quad (5)$$

n_r and n_s are the total number members x_r and x_s in the clusters r and s respectively.

To make sure that only one representation of a mode is present in each cluster, repeated poles at single model orders are sought out and all but the one with the highest proximity to the cluster centroid according to Eq. (1) are removed.

Outlier detection is used remove any remaining frequency or damping ratio outliers in the individual clusters. Here the modified Thompson Tau technique is used [9].

The choice of physical clusters

Two types of clusters will be created by the hierarchical clustering process: Large clusters that represent physical system modes and small clusters consisting of fictitious modes. The examination of the present data showed that the gap between physical and fictitious sets spans a region from approximately 75% to 25% of the largest set size in the majority of the investigated datasets. Thus, a minimum cluster size of 50% is used.

Final modal representation

Each processed physical cluster contains a large number of modes. Hence, the questions arises how to choose a single representation of the individual modal properties. In this work the mean values are used, which are calculated according to Eq. (6) and Eq. (7).

$$\bar{\lambda}_k = \frac{1}{N} \sum_{i=1}^{N} \lambda_{k,i} \quad (6)$$

Here $\lambda_{k,i}$ is the pole from the ith model order in cluster k and $\bar{\lambda}_k$ is the mean cluster pole. The mean cluster mode shape $\bar{\boldsymbol{\phi}}_k$ is calculated according to

$$\begin{aligned} \mathbf{USV}^T &= \left[\boldsymbol{\phi}_{k,1}, \dots, \boldsymbol{\phi}_{k,N}\right] \\ \bar{\boldsymbol{\phi}}_k &= \boldsymbol{U}[\boldsymbol{:}, \mathbf{1}] \end{aligned} \quad (7)$$

where $\boldsymbol{U}[\boldsymbol{:}, \mathbf{1}]$ is the first column vector of the unitary matrix $\boldsymbol{U}$, which in turn is calculated from the Singular Value Decomposition (SVD) of all mode shapes $\boldsymbol{\phi}_{k,1}, \dots, \boldsymbol{\phi}_{k,N}$ in cluster k.

Automated baseline preparation

The number of modes identified from each dataset with the algorithm presented in section 2.2 is indeterminate and they are not grouped in any way.

The goal of the automated baseline generation procedure is to single out consistently identified modes from every baseline dataset and order them into cohesive sets. The end product of the procedure is the $N \times p$ matrix $\mathbf{X}$, where each row of $\mathbf{X}$ represents one measurement of the feature vector x_i^T. p is the number of features extracted from the selected modal properties. This problem has a lot in common with the task of detecting consistency throughout different model orders. Hence, some steps in the subsequently described algorithm are similar to the steps described in section 2.2.

The procedure starts with AOMA identifications from a large number of baseline datasets M, where $m = 1, 2, \ldots, M$. Each AOMA baseline dataset consists of K_m poles $\lambda_1 \ldots \lambda_{K_m}$ and K_m unscaled mode shapes $\boldsymbol{\phi}_1 \ldots \boldsymbol{\phi}_{K_m}$. The number of modes K_m identified with AOMA may vary from dataset to dataset. Before the AOMA data are processed they may have to be randomly shuffled on the dataset scale. This will allow to account for sudden changes of Operational and Environmental Conditions (OEC) which otherwise may be identified as separate modes. In the case of the present dataset shuffling is required since only stepwise operational changes were measured.

In the next step every mode is associated with its nearest neighbour from the following dataset. The approach is identical to the one described in section 2.2.1. However, instead of different model orders different datasets are used in Eq. (1). Consistently identified modes will have nearest neighbours in near proximity to them, whereas modes that are not consistently identified, false identifications or modes that are only identified at certain OEC will tend to have significantly larger distances to the nearest neighbour.

Next, the observations are separated into a small-distance and a large-distance set similar to the step described in section 2.2.2. However, since it is expected that the AOMA procedure works well and the majority of observations comes from modes that are well excited and consistently identified a clustering procedure has to be used that works with clusters of different size. Again, the

SVC-vector introduced in Eq. (2) is used to separate between small-distance and large-distance observations. The features are again transformed and normalized . However, instead of k-means clustering a Gaussian Mixture Model (GMM) is used (Eq. (8)).

$$p(\boldsymbol{h_N}) = \sum_{k=1}^{2} \pi_k \mathcal{N}\left(\boldsymbol{h_N}|\boldsymbol{\mu_k}, \boldsymbol{\Sigma_k}\right) \qquad (8)$$

$$\text{where } 0 < \pi_k < 1, \ \sum_{k=1}^{2} \pi_k = 1$$

The cluster centroids $\boldsymbol{\mu_1}$ and $\boldsymbol{\mu_2}$ are initialized with $-\mathbf{1}$ and $+\mathbf{2}$ respectively. Furthermore, $\pi_1 = 0.9$ and $\pi_2 = 0.1$ are used as initial weights. The covariance matrices $\boldsymbol{\Sigma_1}$ and $\boldsymbol{\Sigma_2}$ are initialized using $\boldsymbol{I}$ and $0.1 \cdot \boldsymbol{I}$ respectively, where $\boldsymbol{I}$ is the identity matrix. The result of the clustering procedure will be two sets S_1 and S_2 that contain the modes with low-distance neighbours and large-distance neighbours.

Hierarchical clustering is used to sort the observations into consistent sets. The cutoff distance is again derived from Eq. (4). However, here the 99th percentile is used to account for possible OEV. Again the modified Thompson Tau technique is used to remove natural frequency and damping ratio outliers in the sets $S_{hc,m}$ returned by the hierarchical clustering procedure.

There exists a tradeoff between the number of modes that can be used for subsequent damage detection and the percentage of baseline datasets that are feature-complete, i.e. have an observation in every cluster $S_{hc,m}$. The ratio between the number of observation $M_{hc,m}$ in a cluster $S_{hc,m}$ and the total number of baseline datasets M can be used as a threshold to control this tradeoff.

$$\vartheta \leq \frac{M_{hc,m}}{M} \qquad (9)$$

Only the K_{fc} clusters with a minimum number of objects $\vartheta \cdot M$ are retained for subsequent analysis.

The final step of the baseline data preparation procedure is to remove all datasets that do not have a representative in each remaining cluster. The

number of feature-complete baseline datasets is $N \leq M_{hc,m}$. These N datasets are used to extract the p individual features for the feature vector X that are used for subsequent damage detection. In this work natural frequencies and damping ratios are used as features. Hence, one row x_i^T of the feature matrix X is defined as

$$x_i = [\, f_{u,i,1}, \ldots, f_{u,i,K_{fc}}, \xi_{u,i,1}, \ldots, \xi_{u,i,K_{fc}} \,]^T \qquad (10)$$

where $f_{u,i,1}, \ldots, f_{u,i,K_{fc}}$ are the K_{fc} natural frequencies extracted from the ith feature-complete dataset. $\xi_{u,i,1}, \ldots, \xi_{u,i,K_{fc}}$ are the damping ratios extracted from the same dataset.

Modal tracking

The baseline preparation procedure outlined in section 2.3 returns K_{fc} clusters of consistently identified modes. In SHM newly arriving measurements are compared to the baseline dataset or training model to examine whether the dataset represents an anomaly or not. Since the number of modes identified from the newly arriving dataset is again indeterminate and the presence of modes that were selected for the baseline set is not guaranteed, a procedure is needed that matches modes identified from the new dataset with modes that were selected for the baseline dataset.

First, if the number of modes in the new dataset M_{new} is smaller than the number of modes in the baseline K_{fc}, the dataset is skipped. In the next step the distance according to Eq. (1) between each mean baseline mode k and every mode in the new dataset l is calculated. This results in a $K_{fc} \times M_{new}$ dpMAC distance matrix D_{MT}, where $K_{fc} \leq M_{new}$. The affiliation between the pair of modes $\bar{\lambda}_k, \bar{\phi}_k$ and $\lambda_{new,l}, \phi_{new,l}$ with the smallest dpMAC distance $D_{MT,k,l}$ is saved. The mean baseline poles $\bar{\lambda}_k$ and modes shapes $\bar{\phi}_k$ are calculated according to Eq. (6) and Eq. (7) respectively. The corresponding row k and column l are removed from the distance matrix D_{MT}. The procedure is repeated until a mode from the new dataset was associated with every baseline cluster.

Damage detection

Anomalies are detected using the Mahalanobis distance, which is defined according to Eq. (11).

$$d_m = \sqrt{\left(x_n - \hat{\mu}_{BL}\right)^T \hat{\Sigma}_{BL}^{-1} \left(x_n - \hat{\mu}_{BL}\right)} \qquad (11)$$

where $\hat{\Sigma}_{BL}$ is the covariance matrix estimate of the baseline feature vector X, x_n is the to be tested observation and $\hat{\mu}_{BL}$ is the mean of each individual feature in X.

Results and Discussion

The first data-processing step in SHM is damage-sensitive feature extraction. Figure 4 shows the results of the AOMA algorithm (section 2.2) applied to a single FBG dataset. The modal parameters were identified in the model order range $n = \{2, 4, 6, \ldots, 100\}$. Eight consistently identified modes were flagged as physical. The vast majority of mode candidates were classified as fictitious. Out of the eight physical modes, four can be assigned to physical system modes in the shown frequency range, two are the result of a wind tunnel induced excitation and two can be explained with the non-existing anti aliasing filter of the optical interrogator. See [4] for a more thorough discussion of the wind-induced phenomena and the limitations of the optical sensing system.

The raw AOMA identifications have to be further processed to extract, select and arrange the features in a way that makes them suitable for subsequent SHM. Figure 5 shows over 1000 AOMA identifications from the piezoelectric measurements. All datasets labeled as Baseline were processed with the algorithm described in section 2.3. A consistency threshold of 90% was chosen (Eq. (9)). Eight modes were identified with higher than required consistency. These were selected as features and are marked with colors in figure 5. The observations in Test and Damaged were assigned to the corresponding features using the modal tracking algorithm described in section 2.4. Thus, a training set was automatically created that is suitable for subsequent one-class classification or anomaly detection.
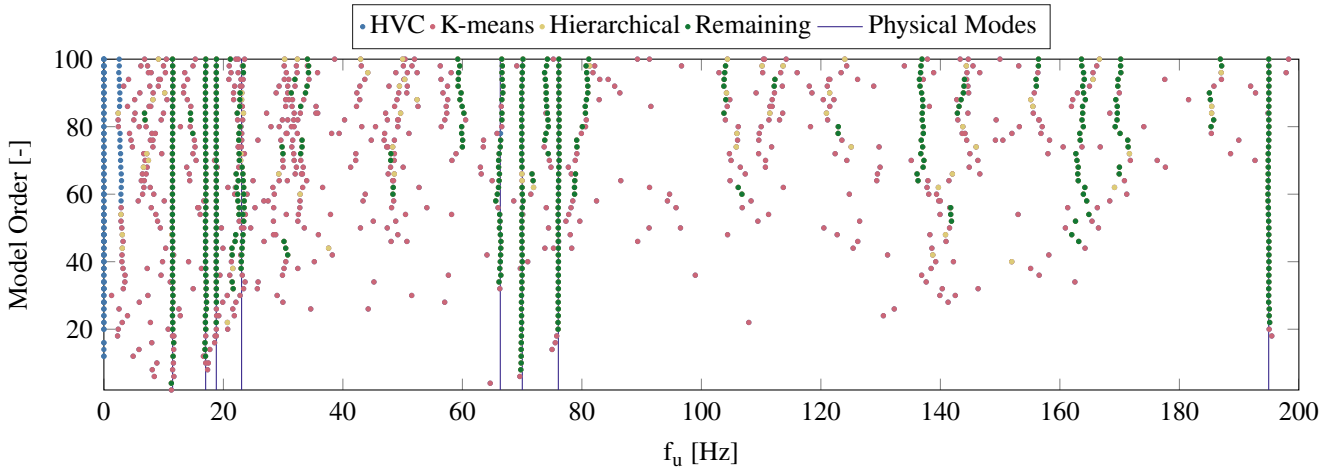
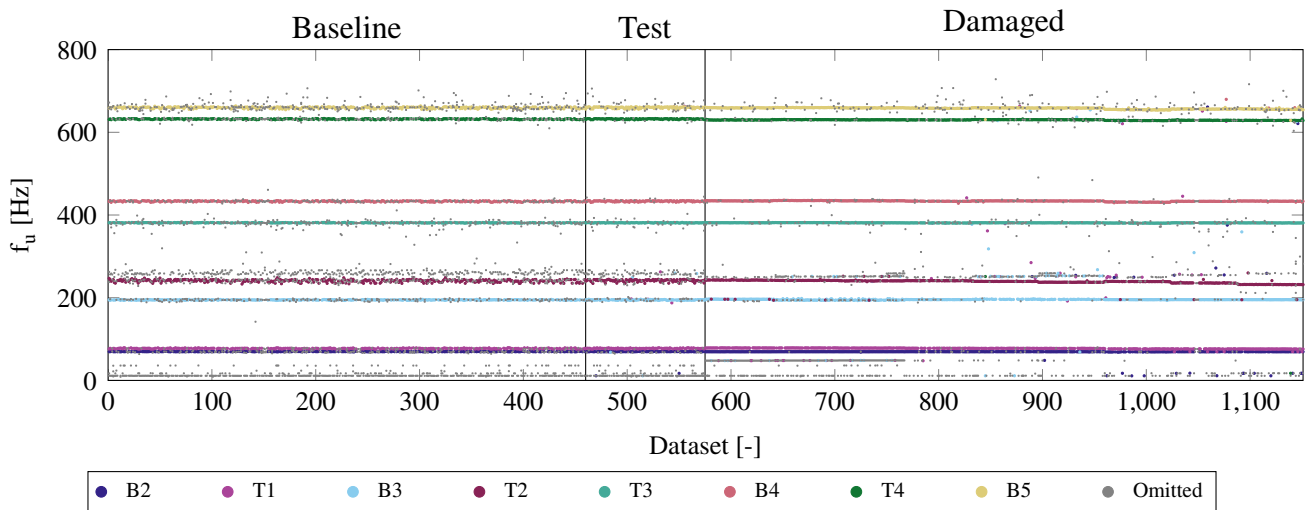Figure 4: Stabilisation diagram from Fiber Bragg Grating Sensorss (FBGSs)

Figure 5: Natural frequencies identified with the AOMA algorithm from piezoelectric data. Representations of a single mode that were selected for the feature vector are highlighted with colors and denoted with their respective type of movement (where B stands for bending and T for torsion).

The first SHM level is damage detection (I). Initially, the Baseline data prepared with the approach described in section 2.3 are used to learn $\hat{\Sigma}_{BL}$ and $\hat{\mu}_{BL}$, the parameters of Eq. (11). Next, the distance between every observation in Baseline, Test and Damaged and the Baseline mean according to (11) is determined. Figure 6 shows the results of this investigation. The damage is clearly detectable under full velocity and AOA variability. The false alarm rate of the procedure can be controlled by taking advantage of the fact that once damage occurs it does not go away. Thus, multiple successive outliers are a sure sign of an anomaly.
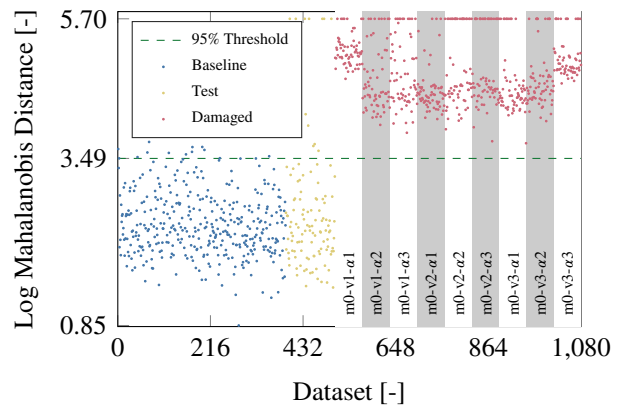

Figure 6: Damage detection at a constant mass m_0 but otherwise unmeasured OEC.

The next SHM level is damage localisation (II). Its theoretical feasibility was demonstrated using mode shape related quantities like Strain Mode Shapes (SMSs) in a number of studies [10]. However, these results were achieved either numerically or under laboratory conditions and without the influence of OEV. Figure 7 shows the SMS differences along Path A (figure 3) of the FEM model. Comparable results can be obtained for the other SMS. The results show that damage localisation is clearly possible under ideal conditions, even if the practical implementation remains open to debate.
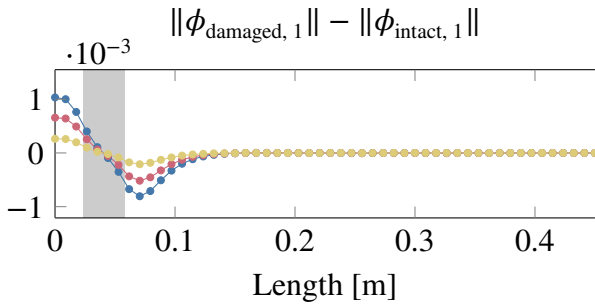
(a) First bending mode (B1) delamination.
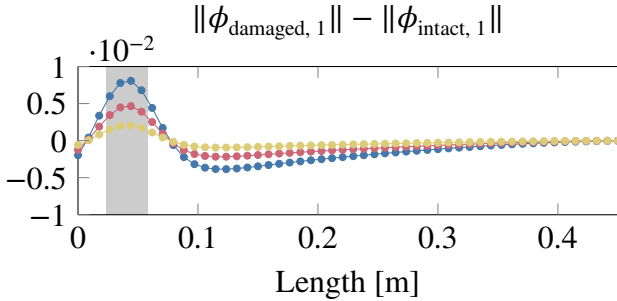
(b) First bending mode (B1) stiffness reduction.

Figure 7: Numerical model SMS differences for varying damage severities. The damaged area is gray-shaded.

The comparatively dense optical sensor distribution at the surface of the investigated specimen would theoretically have allowed for damage localisation. Figure 8 shows the identification variability of the first bending mode SMS for a single FBGS. The different OECs build distinguishable but strongly overlapping clusters. The picture is even worse for other FBGS and modes. Hence, the limited sampling frequency and the comparatively low sensitivity of the used interrogator made damage localisation from FBG data not feasible. The piezoelectric data show much lower variance under constant OEC. However, the number of piezoelectric sensors used was too low for damage localisation. Thus, vibration-based damage localisation under OEV seems to be feasible provided that a dense network of highly sensitive sensors is available. However, further research is necessary to include localisation data into a statistical framework that is able to account for uncertainly and OEV. Currently the vast majority of methods proposed for damage localisation are not formulated in such a way [10].
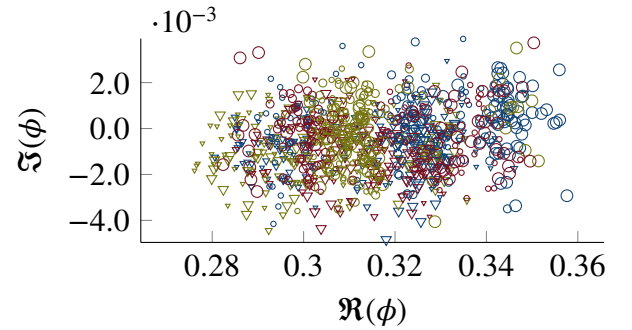

Figure 8: First bending mode SMS at 7th FBG sensor. $\circ$/ $\triangledown$ represent damaged/normal samples. Symbol size increases from m_0 to m_2. Colors represent different AOAs.

Table 1 shows damage-induced natural frequency shifts under operational variability. Each table field was calculated according to Eq. (12).

$$df_i = \frac{\bar{f}_{u,d0,i} - \bar{f}_{u,d1,i}}{\bar{f}_{u,d0,i}} \tag{12}$$

$\bar{f}_{u,d0,i}$ is the mean undamaged natural frequency of mode i under the operational conditions given in the first column of the table. Accordingly $\bar{f}_{u,d1,i}$ is the corresponding damaged mean natural frequency. All data are given as percentages. The damage-induced frequency shifts are quite small. They rarely exceed 1% of the undamaged natural frequency. In contrast, mass and velocity-induced changes can reach values of over 5% and 3% respectively. For an uncoupled system one would expect consistent damage-induced shifts throughout the different OECs. This is clearly not the case. On the contrary, there seem to be significant interactive terms between the investigated

damage and the encountered OEC. This has consequences for the feasibility of damage type detection (III) and severity estimation (IV) systems. Such systems have to be trained with representative samples of the outlier class [3]. Since comprehensive experimental damage studies of complex engineering structures are prohibitively expensive, a frequently suggested approach is to use numerically generated outlier samples. Table 1 shows that such models not only have to find an appropriate numerical simplification of every frequently encountered damage scenario but also have to consider the effect of OEV. For an aircraft wing this means that, beside the need for a numerical model of every conceivable or critical damage scenario at every possible damage position, there is also the need to model the full operational (and environmental) range. The sheer amount of possible system states and the need to consider multiple nonlinear effects translate to very high computational and methodical demands. Further research is necessary to reduce the complexity of the problem and make damage classification and severity estimation of complex structures under OEV feasible.

Table 1: Natural frequency shifts as a result of the investigated damage under OEV m, v and α.

OEC		B2	T1	B3	T2	T3	B4	T4	B5
m0-v1-α1	[%]	-0.12	0.32	-1.23	0.63	-0.24	0.04	0.40	0.30
m0-v1-α2	[%]	0.15	-0.95	-0.21	0.70	0.10	-0.12	0.35	0.20
m0-v1-α3	[%]	0.20	-0.71	-0.39	1.20	0.12	0.03	0.43	0.37
m0-v2-α1	[%]	-0.52	-0.05	-0.15	0.45	-0.12	0.10	0.45	0.40
m0-v2-α2	[%]	-1.19	-0.28	-0.64	0.81	0.06	-0.14	0.25	0.17
m0-v2-α3	[%]	-0.55	-0.15	-0.46	1.09	0.02	-0.18	0.29	0.20
m0-v3-α1	[%]	1.21	0.04	-0.26	0.52	-0.19	-0.00	0.38	0.30
m0-v3-α2	[%]	0.65	-0.11	-0.27	0.80	-0.23	-0.26	0.28	0.21
m0-v3-α3	[%]	0.19	-0.14	-0.38	1.57	-0.35	-0.43	0.26	0.13
m1-v1-α1	[%]	0.06	-1.10	-0.21	0.20	0.06	-0.23	0.29	0.22
m1-v1-α2	[%]	0.20	-0.96	0.10	0.66	-0.10	-0.05	0.27	0.26
m1-v1-α3	[%]	0.17	-0.93	0.09	0.78	-0.16	-0.15	0.32	0.32
m1-v2-α1	[%]	-0.27	-0.48	-0.18	0.13	0.02	-0.36	0.18	-0.04
m1-v2-α2	[%]	-0.43	-0.74	-0.57	0.72	-0.03	-0.35	0.17	-0.04
m1-v2-α3	[%]	-0.28	-0.37	-0.65	1.21	-0.28	-0.30	0.25	0.29
m1-v3-α1	[%]	0.83	-0.70	-0.42	0.04	-0.26	-0.56	0.19	-0.13
m1-v3-α2	[%]	0.22	-0.24	-0.36	0.84	-0.14	-0.41	0.26	0.14
m1-v3-α3	[%]	-0.73	-0.33	-0.39	1.20	-0.23	-0.58	0.20	-0.10
m2-v1-α1	[%]	-0.31	-1.15	-0.42	0.31	-0.26	-0.20	0.27	0.16
m2-v1-α2	[%]	-0.23	-1.16	-0.13	0.67	-0.16	-0.14	0.24	0.18
m2-v1-α3	[%]	-0.11	-1.18	-0.00	0.95	-0.00	-0.13	0.28	0.25
m2-v2-α1	[%]	0.35	-0.19	0.13	0.38	0.07	0.01	0.23	0.24
m2-v2-α2	[%]	-0.33	-0.71	0.10	0.51	-0.29	-0.45	0.18	-0.03
m2-v2-α3	[%]	-0.17	-0.15	-0.31	1.29	-0.18	-0.13	0.35	0.26
m2-v3-α1	[%]	0.17	-0.52	-0.33	0.08	-0.16	-0.43	0.26	-0.02
m2-v3-α2	[%]	-0.38	-0.19	-0.32	0.77	-0.23	-0.40	0.27	-0.01
m2-v3-α3	[%]	-0.30	0.49	-0.24	1.74	-0.03	-0.18	0.35	0.26

Figure 9 shows a correlation coefficient matrix. The correlation coefficients were calculated between the damage-induced shifts of the eight natural frequencies selected by the algorithm described in section 2.3 and the corresponding natural frequency shifts of the numerical models. Only data from a single mass configuration m_0 were considered. One can derive from the significantly higher correlation coefficients that the stiffness reduction is a better representation of the investigated impact damage than pure delamination. Furthermore, the data shows that correlation drops substantially with increasing influence of the OEV. This results further substantiate the fact that damage and OEV-induced feature changes are not independent. A combination of the two damage scenarios may further improve the correlation between the experimental and numerical results. This scenario was not investigated.

Figure 9: Correlation coefficients between damage-induced natural frequency changes under operational variability and as a result of two numeric damage scenarios. d1-X $\hat{=}$ delamination, d2-X $\hat{=}$ stiffness reduction, X $\hat{=}$ damage severity.

To advance vibration-based SHM in the context of aircraft wings a number of open questions have to be answered and multiple challenges have to be overcome. The effects of possibly critical damage scenarios on the global modal properties of wings needs to be studied numerically and experimentally. Huge amounts of in-flight vibration data, acquired under realistic operational and environmental conditions, are needed to assess whether critical wing damage can be detected (and localised) using vibration-based SHM methods. Fiber optic sensing, which remains the

most promising technology for the task, improved impressively over the last two decades and still needs to improve considerably to fulfill the requirements imposed upon it. The general feasibility of vibration-based SHM is tested and proven. However, the application to an aircraft wing under full operational and environmental variability is a formidable challenge for the decade to come.

Conclusion

A fully automated method for vibration-based SHM methodology that is developed for in-flight monitoring of wings was presented and successfully tested on a composite cantilever specimen, which was subjected to wind-induced operational variability in a wind tunnel. A small scale impact damage was introduced to the specimen and successfully detected using the proposed method.

Damage localisation from vibration-based SHM was shown to be generally feasible. However, the FBG interrogator utilised in this study turned out to be not sensitive enough for this task.

It was shown that damage-induced feature vector changes and changes introduced by operational and environmental variability cannot be considered independently. The discussion revealed this to be a strong barrier to the introduction of SHM systems that go beyond damage detection and localisation. The results were discussed in the context of aircraft wings.

References

[1] Worden, K., Farrar, C. R., Manson, G., and Park, G. "The Fundamental Axioms of Structural Health Monitoring". *Proceedings of the Royal Society A: Mathematical, Physical and Engineering Sciences* 463.2082 (2007), pp. 1639–1664.

[2] Magalhães, F., Cunha, A., and Caetano, E. "Vibration based Structural Health Monitoring of an Arch Bridge: From Automated OMA to Damage Detection". *Mechanical Systems and Signal Processing* 28 (2012), pp. 212–228.

[3] Farrar, C. R. and Worden, K. *Structural Health Monitoring: A Machine Learning Perspective*. Chichester, United Kingdom: John Wiley & Sons, Ltd, 2012.

[4] Neu, E., Janser, F., Khatibi, A. A., and Orifici, A. C. "Operational Modal Analysis of a Cantilever in a Wind Tunnel using Optical Fiber Bragg Grating Sensors". In: *Proceedings of the 6th International Operational Modal Analysis Conference*. Gijón, Spain, 2015.

[5] Overschee, P. v. and Moor, B. L. R. d. *Subspace Identification for Linear Systems: Theory, Implementation, Applications*. Boston, USA: Kluwer Academic, 1996.

[6] Reynders, E., Houbrechts, J., and Roeck, G. de. "Fully Automated (Operational) Modal Analysis". *Mechanical Systems and Signal Processing* 29 (2012), pp. 228–250.

[7] Box, G. E. P. and Cox, D. R. "An Analysis of Transformations". *Journal of the Royal Statistical Society. Series B (Methodological)* 26.2 (1964), p 211–252.

[8] Hastie, T., Tibshirani, R., and Friedman, J. H. *The Elements of Statistical Learning: Data Mining, Inference, and Prediction*. 2nd. New York, USA: Springer, 2009.

[9] Cimbala, J. M. *Outliers: Lecture on Instrumentation, Measurements, and Statistics*. Accessed: 12 Juli, 2016. State College, Pennsylvania, USA, 2011.

[10] Montalvao, D. "A Review of Vibration-based Structural Health Monitoring with Special Emphasis on Composite Materials". *The Shock and Vibration Digest* 38.4 (2006), pp. 295–324.

Copyright Statement